Supplement of Geochronology, 8, 297–312, 2026
https://doi.org/10.5194/gchron-8-297-2026-supplement

Supplement of

Novel insights into the post-IR $IRSL_{200}$ signal bleachability of single-grain K-feldspars in fluvial modern analogues from the Southern Central Andes, Chile

Arindam Biswas et al.

Correspondence to: Arindam Biswas (abiswas3@uni-koeln.de)

Supplementary materials

List of contents

S1: Catchment properties

To calculate the mean rainfall for each catchment (Table S2), the time-averaged map of daily accumulated precipitation (combined microwave-IR) estimate [GPM_3IMERGDF v06] (Huffman et al., 2023) dataset was utilised. This dataset, spanning the period from January 1, 2001, to December 31, 2019, provides high-resolution precipitation estimates derived from a combination of microwave and infrared measurements. The data was obtained from NASA's Giovanni application, an online tool for accessing and analysing Earth science data. By aggregating daily precipitation values over these 19 years, spatially averaged rainfall data for each catchment were obtained. This approach ensured a robust representation of mean precipitation patterns, accounting for temporal variability and spatial heterogeneity within the study region.

NDVI data were processed using the Google Earth Engine platform (Gorelick et al., 2017). The analysis incorporated Landsat 8 surface reflectance data products from January 2002 to January 2022, with necessary pre-processing involving cloud cover filtering, to calculate the NDVI for each catchment. The JavaScript code available for NDVI calculation from Landsat scenes on the Google Earth Engine tutorials platform was used for this purpose.

Topographic analysis was conducted using a 30 meter resolution Digital Elevation Model (DEM) from the NASA Shuttle Radar Topography Mission (2013). The DEM was further processed using ArcGIS software, which includes filling the sinks, delineating all the catchments (sampling locations were considered as outlets for catchment delineation), and also calculating catchment area, mean slope, and mean elevation.

The Randolph Glacier Inventory-A Dataset of Global Glacier Outlines, Version 7.0 (RGI 7.0 Consortium, 2023) was used to delineate glacier cover within each catchment. This dataset enabled the identification and quantification of glacier coverage, providing essential data for understanding the influence of glacial dynamics on catchment hydrology and geomorphology.

Catchment lithologies were derived from the geological map of South America at a scale of 1:5,000,000 (Gómez et al., 2019). Based on the lithological distribution within each catchment, the major litho-units were classified into four categories: granitic, volcanic, sedimentary, and volcano-sedimentary units, regardless of their age. The proportion of each litho-unit within the catchments (Table S1) was quantified through spatial analysis in ArcGIS software.

Table S1: Details of all eleven samples include sampling location (latitude and longitude), altitude of sampling location, sampling depth, and proportion of the four major lithological units within each catchment. Samples are listed from north to south, CHLEA-11 being the northernmost and CHLEA-5 being the southernmost sample.

Sample ID	Latitude	Longitude	Altitude (m)	Sampling depth (cm)	Granite (%)	Volcanic (%)	Sedimentary (%)	Volcano-sedimentary (%)
CHLEA-11	-28.70	-70.56	656.00	5	67	22	2	9
CHLEA-1	-31.67	-71.29	158.00	20	45	8	10	37
CHLEA-8	-32.85	-70.50	955.00	6	0	28	10	62
CHLEA-6	-33.59	-70.39	861.00	3	0	53	10	37
CHLEA-7	-34.21	-70.53	778.00	11	0	21	19	60
CHLEA-10	-34.68	-70.87	484.00	4	17	0	27	56
CHLEA-3	-35.00	-70.83	633.00	4	0	0	13	87
CHLEA-2	-35.18	-71.12	422.00	3	0	30	5	65
CHLEA-4	-35.73	-71.02	562.00	3	24	9	4	63
CHLEA-9	-36.48	-71.76	275.00	4	2	11	65	22
CHLEA-5	-38.94	-71.92	383.00	7	0	51	49	0

Table S2: Data for each catchment in this study include total catchment area, mean catchment slope, mean catchment elevation, percent glacier-covered area, mean normalised difference vegetation index (NDVI), and daily average rainfall.

Sample ID	Catchment	Total area (km^2)	Mean slope (degrees)	Mean elevation (meters)	Glacier area (%)	Mean NDVI	Daily average rainfall (mm)
CHLEA-11	Huasco	7258.37	24.46	3378.99	0.435	0.045	0.34
CHLEA-1	Choapa	5883.15	21.38	2026.08	0	0.085	0.68
CHLEA-8	Aconcagua	2100.09	27.98	3174.8	1.667	0.044	1.17
CHLEA-6	Maipo	4864.59	27.56	3182.09	7.195	0.045	1.86
CHLEA-7	Cachapoal	2411.37	27.43	2680.82	6.612	0.045	2.41
CHLEA-10	Tinguiririca	1838.26	25.58	2328.85	4.225	0.089	2.56
CHLEA-3	Teno	1208.22	26.42	2090.45	0.093	0.102	2.99
CHLEA-2	Lontué	1781.09	19.8	1940.19	0.156	0.125	2.85
CHLEA-4	Maule	2706.2	21.32	2207.62	0.31	0.068	2.68
CHLEA-9	Ñuble	1864.96	22.69	1492.36	0.789	0.21	3.49
CHLEA-5	Allipén	1372.42	17.73	1158.29	3.092	0.281	4.06

S2: Details of preheat plateau and dose recovery test

S2.1: Multi-grain

For multigrain dose-recovery and residual preheat plateau tests, eight aliquots (aliquot size = 2 mm) were bleached for 2 days in the laboratory solar simulator (Sol2) for each preheat temperature examined. Four of these were used for a dose recovery test (given dose: 30 Gy), and the remaining four aliquots were used for measuring the residual dose. Preheat temperatures ranged from 150 °C to 275 °C at intervals of 25 °C. All the measurements were carried out following the protocol outlined in Table S3. All post-IR IRSL measurements at elevated temperatures were performed at 25 °C lower than their corresponding preheat temperature (Table S4).

Over the range of preheat and post-IR IRSL stimulation temperatures tested, dose recovery ratios (DRRs) were calculated for all steps (Fig. S1a). DRRs were determined after subtracting the average residual dose from the average measured dose of all accepted aliquots, following the acceptance criteria analogous to those applied for single-grain measurements as outlined in Section 2.3 of the main text. CHLEA-11 showed good dose recovery results for all post-IR IRSL signals, while CHLEA-6 exhibited satisfactory dose recovery only for the post-IR $IRSL_{175}$ and post-IR $IRSL_{200}$ signals. Among them, the DRR for the post-IR $IRSL_{200}$ signal (with the preheat temperature of 225 °C) yielded the best result for both samples. The post-IR $IRSL_{200}$ DRRs for CHLEA-11 and CHLEA-6 were 0.98 ± 0.05 and 0.98 ± 0.06 respectively, well within the range of 0.90 to 1.10 (unity ± 10%). Thus, the post-IR $IRSL_{200}$ signal was selected for further analysis.

S2.2: Single-grain

Once the protocol was established using multi-grain aliquots, individual K-feldspar grains were loaded into single-grain discs with 300 µm holes to perform a dose recovery test, assessing the suitability of the protocol at the single-grain level on four samples (CHLEA-11, CHLEA-6, CHLEA-10, and CHLEA-9). The protocol described in Table S3 (for single-grain) was used for post-IR $IRSL_{200}$ signal measurement and analysis. Grains were bleached for 2 days in the Sol2 prior to measurement. 5 to 16 single-grain discs (equivalent to 500 to 1600 grains) were measured for both residual dose measurement and dose recovery tests (given dose: 30 Gy). The residual subtracted DRRs of the four samples were 0.87 ± 0.02, 0.88 ± 0.06, 0.93 ± 0.06, and 0.84 ± 0.07 respectively (Fig. S2).

Table S3: Post-IR IRSL measurement protocol of dose recovery and residual preheat plateau test on multigrain aliquots and single-grain (SG) dose recovery tests. [a]For the dose recovery test, the given dose was 30 Gy with regenerative doses of 0, 10, 20, 30, and 50 Gy and a [c]test dose of 20 Gy. [b]For residual dose measurement, regenerative doses of 0, 2, 5, 10, and 30 Gy were applied, with a [c]test dose of 10 Gy. The range of preheat temperatures used was X = 150, 175, 200, 225, 250, and 275. The post-IR IRSL stimulation temperature was always 25 °C lower than the applied preheat temperature (i.e., X-25). Post-IR $IRSL_{200}$ was measured for the single-grain dose recovery test. Note that single-grain dose recovery tests include an additional step (IR LEDs at 200 °C, 300 s) between steps 8 and 9.

Step	Treatment	Observed
1	Beta dose[a,b]	
2	Preheat at X °C, 60 s	
3	IRSL at 50 °C, 200 s (2 s for SG)	
4	post-IR IRSL at (X-25) °C, 300 s (3 s for SG)	L_x
5	Test dose[c]	
6	Preheat at X °C, 60 s	
7	IRSL at 50 °C, 200 s (2 s for SG)	
8	post-IR IRSL at (X-25) °C, 300 s (3 s for SG)	T_x
9	Repeat steps 1 to 8 for a range of regenerative doses (incl. zero and repeat dose, zero dose measured after the largest regenerative dose)	

Table S4: Preheat and post-IR IRSL stimulation temperature combinations of multi-grain dose recovery and residual preheat plateau test.

Preheat stimulation temperature (°C)	Post-IR IRSL stimulation temperature (°C)
150	125
175	150
200	175
225	200
250	225
275	250

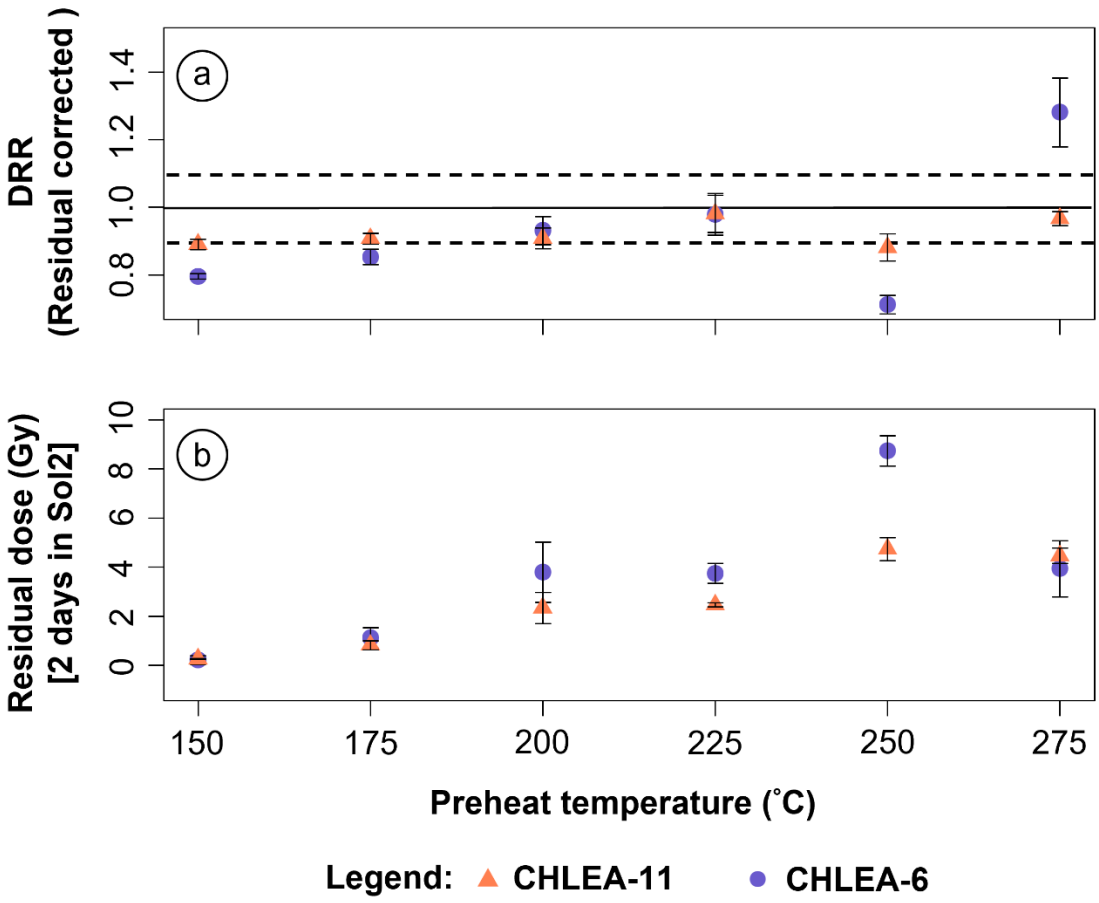

Fig. S1: Results of the dose recovery and residual preheat plateau test performed on samples CHLEA-11 and CHLEA-6 using multi-grain aliquots. (a) Residual corrected dose recovery ratios (DRRs) and (b) residual dose (Gy) estimates, calculated at each preheat temperature. Each data point on both plots represents the average of accepted aliquots. Note that post-IR IRSL stimulation temperature was always 25 °C lower than the applied preheat stimulation temperature. All uncertainties are indicated as one standard error.

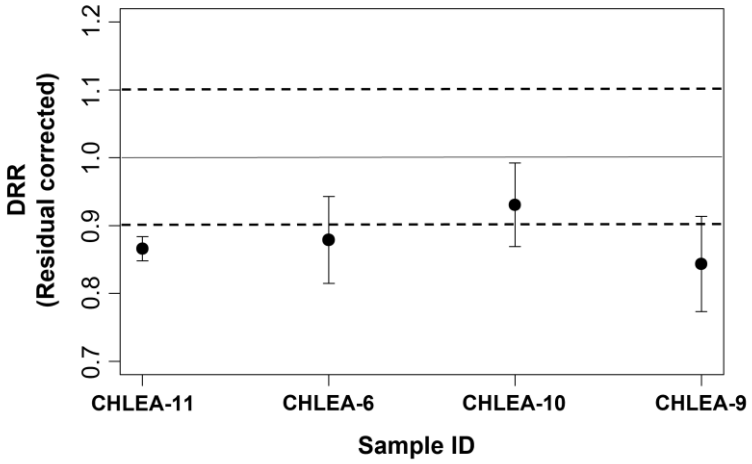

Fig. S2: Residual corrected dose recovery ratios (DRRs) of samples CHLEA-11, CHLEA-6, CHLEA-10, and CHLEA-9 performed at the single-grain level. All uncertainties are indicated as one standard error.

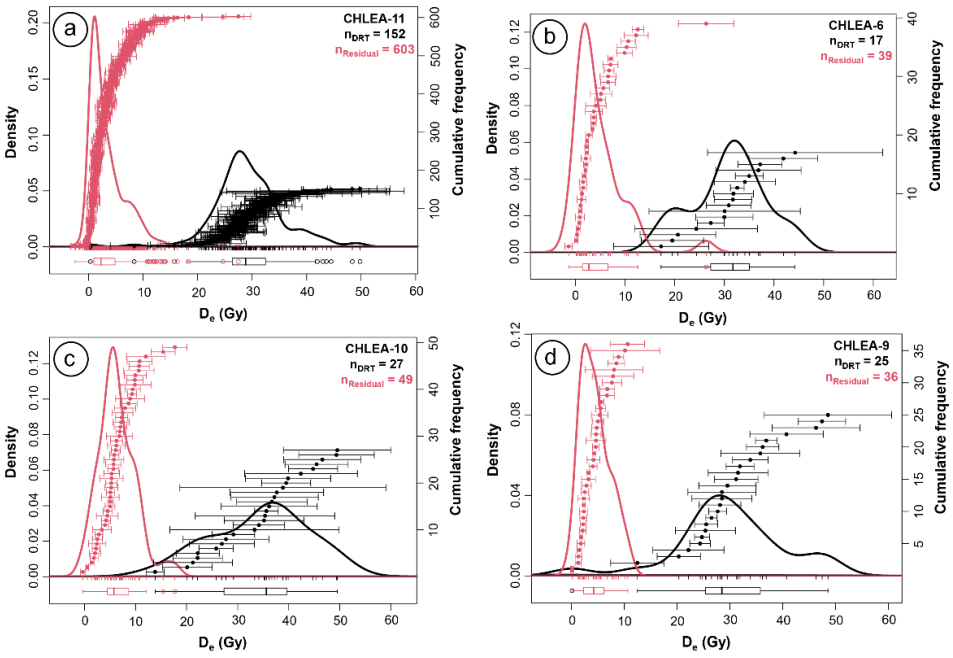

135

Fig. S3: Kernel density estimate plot of all four samples subjected to single-grain dose recovery test and corresponding residual dose measurement. plot_KDE() (Dietze, M., 2023) function of the R-Luminescence package was used to make plots of kernel density estimates shown here using default bandwidth of nrd0 (Silverman, 1998). In all panels, n_{DRT} and $n_{Residual}$ represent the number of grains accepted from the dose recovery test and residual dose
140 **measurement, respectively.**

S3: Details of ancillary luminescence data

S3.1: Luminescence decay and dose response curves

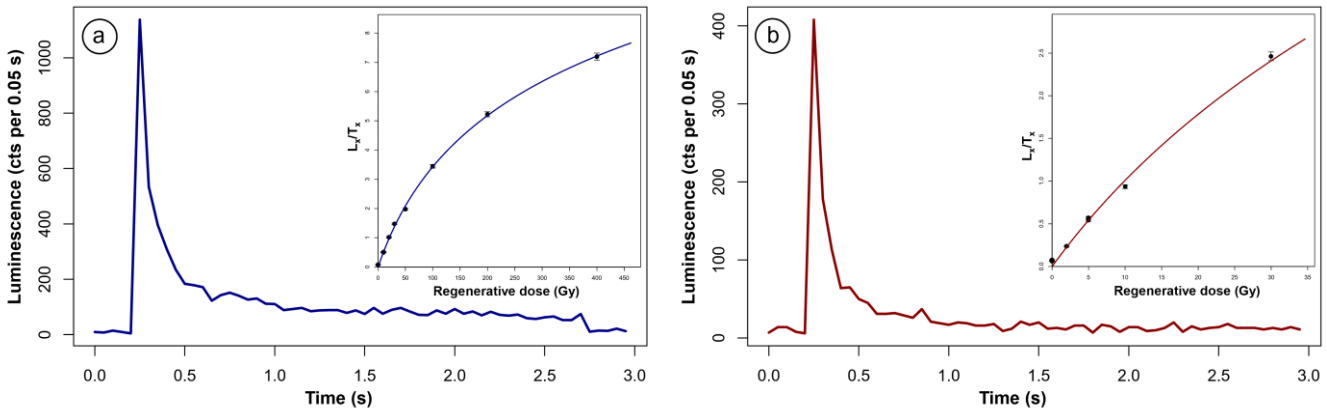

Fig. S4: Examples of single-grain luminescence decay curves and dose response curves of post-IR IRSL$_{200}$ signal from equivalent dose (a) and residual dose (b) measurement. The net post-IR IRSL$_{200}$ signal was calculated from the signal integrated over the first 0.25 s (from the initial part of the decay curve) with subtraction of the background estimated from the last 0.50 s.

S3.2: Summary statistics of accepted and rejected grains

Table S5: Summary of single-grain post-IR $IRSL_{200}$ quality control criteria and rejection statistics for equivalent dose measurements. $n_{Measured}$ = total number of grains analyzed; $n_{Accepted}$ = grains passing all quality criteria; $n_{Total\ rejected}$ = sum of all rejected grains. Rejection criteria include: test dose signal below 3σ background (T_n < 3σ BG), relative standard error of test dose exceeding 20% (RSE of T_n > 20%), recycling ratio (RR) outside unity ± 20%, and figure of merit (FOM) exceeding 15%. Additional rejection statistics in the numOSL package include failed dose-response curve fitting, saturated in natural signal (L_n/T_n), failed D_e error calculation, and failed interpolation onto the growth curve.

Sample ID	$n_{Measured}$	$n_{Accepted}$	T_n< 3σ BG	RSE of T_n> 20%	RR (unity ± 20%)	FOM (15%)	Failed in growth curve fitting	Saturated (L_n/T_n)	Failed in D_e error calculation	Failed by interpolation	$n_{Total\ rejected}$
CHLEA-11	500	307	72	63	12	44	0	0	0	2	193
CHLEA-1	500	109	249	103	13	22	1	1	0	2	391
CHLEA-8	2900	52	2384	408	7	45	0	1	0	3	2848
CHLEA-6	2100	78	1499	432	12	76	0	0	0	3	2022
CHLEA-7	500	262	129	52	8	48	0	0	0	1	238
CHLEA-10	500	66	303	94	2	33	1	0	0	1	434
CHLEA-3	500	78	293	77	4	30	1	2	0	15	422
CHLEA-2	1000	77	760	126	5	23	0	1	2	6	923
CHLEA-4	2700	72	2186	388	13	38	2	0	1	0	2628
CHLEA-9	500	63	314	95	3	18	2	0	1	4	437
CHLEA-5	2000	60	1666	237	8	23	1	1	0	4	1940

Table S6: Summary of single-grain post-IR $IRSL_{200}$ quality control criteria and rejection statistics for residual dose measurements. $n_{Measured}$ = total number of grains analyzed; $n_{Accepted}$ = grains passing all quality criteria; $n_{Total\ rejected}$ = sum of all rejected grains. Primary rejection criteria include: test dose signal below 3σ background (T_n < 3σ BG), relative standard error of test dose exceeding 20% (RSE of T_n > 20%), recycling ratio (RR) outside unity ± 20%, and figure of merit (FOM) exceeding 15%. Additional rejection statistics in the numOSL package include failed dose-response curve fitting, failed D_e error calculation, and failed interpolation onto the growth curve.

Sample ID	$n_{Measured}$	$n_{Accepted}$	T_n< 3σ BG	RSE of T_n> 20%	RR (unity ± 20%)	FOM (15%)	Failed in growth curve fitting	Failed in D_e error calculation	Failed by interpolation	$n_{Total\ rejected}$
CHLEA-11	1600	603	548	267	25	155	2	0	0	997
CHLEA-1	700	92	380	185	1	40	0	1	1	608
CHLEA-8	2200	21	1859	292	3	24	1	0	0	2179
CHLEA-6	1800	39	1348	369	6	38	0	0	0	1761
CHLEA-7	400	132	148	65	6	48	0	1	0	268
CHLEA-10	900	49	546	224	6	68	1	0	6	851
CHLEA-3	500	73	293	95	4	35	0	0	0	427
CHLEA-2	1000	71	723	173	3	28	0	2	0	929
CHLEA-4	1300	43	1059	187	1	10	0	0	0	1257
CHLEA-9	800	36	575	156	2	31	0	0	0	764
CHLEA-5	1800	30	1559	192	1	17	0	1	0	1770

S3.3: KDE plots of D_e and residual dose distribution

Figure S5 presents kernel density estimate plots of single-grain equivalent dose (D_e) and residual dose estimates for some selected samples. Panels (a) and (c) display data for CHLEA-4 and CHLEA-7, while panels (b) and (d) correspond to CHLEA-6 and CHLEA-9. Despite CHLEA-4 and CHLEA-7 originating from catchments with similar dominant lithology (Table S1), their Mode D_e and $Mode_{Residual}$ estimates differ markedly (Table 3, main text). In contrast, CHLEA-6 and CHLEA-9 exhibit comparable Mode D_e and $Mode_{Residual}$ estimates, despite different dominant lithologies (Table S1).

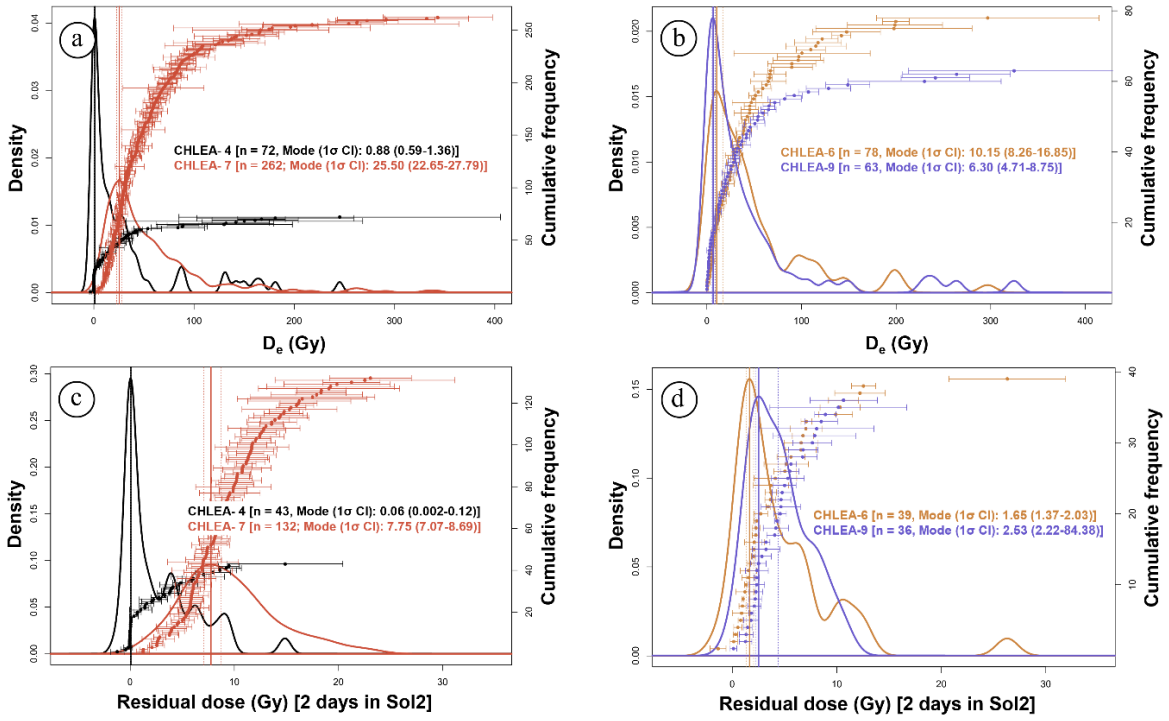

Fig. S5: Examples of kernel density estimate plots of single-grain equivalent dose (D_e) estimates and residual dose estimates for samples CHLEA-4 and CHLEA-7 in panels (a) and (c), respectively; and for samples CHLEA-6 and CHLEA-9 in panels (b) and (d), respectively. All KDE plots were generated using the plot_KDE() function from the R-Luminescence package (Dietze, 2023), with bandwidths determined via the Sheather-Jones method (Sheather and Jones, 1991) to ensure accurate visualisation of distributional modes (solid vertical lines) and bootstrap-derived confidence intervals (dashed vertical lines).

S3.5: Comparing Mean D_e with $Mean_{Residual}$

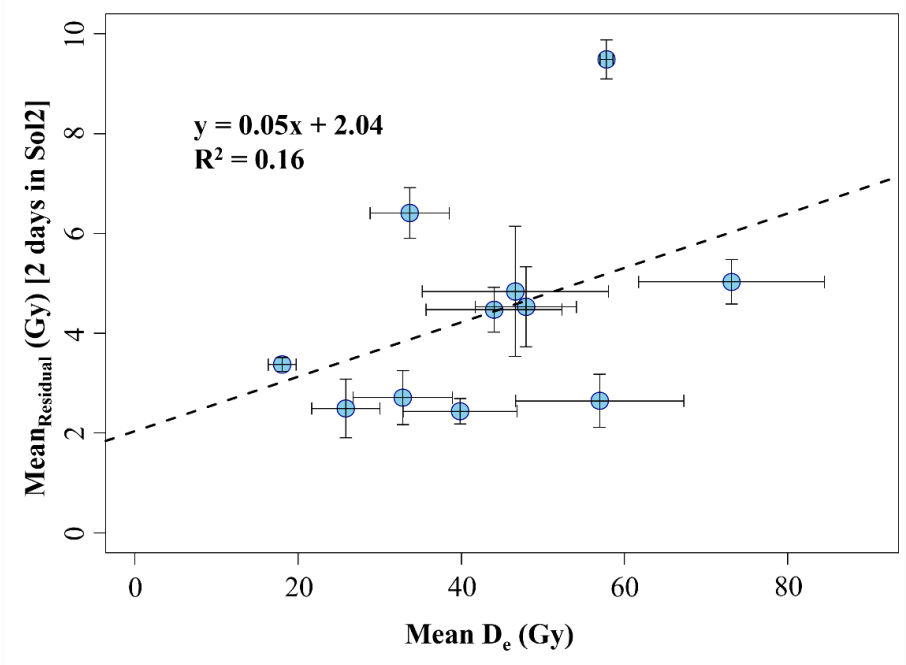

Fig. S6: Plot of Mean D_e versus $Mean_{Residual}$ with a linear fit, fitting equation, and coefficient of correlation.

205 **S4: Associated results of the bleaching experiment**

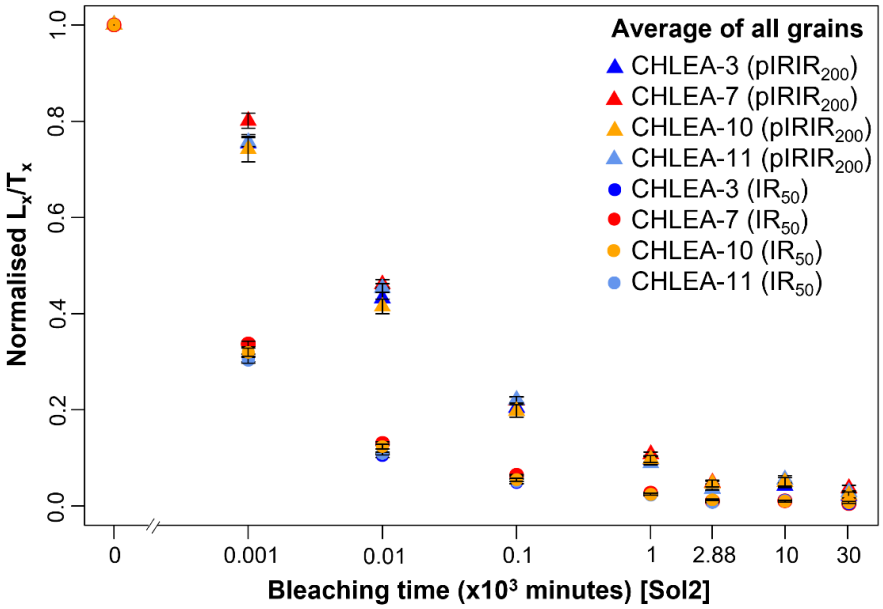

Fig. S7: $IRSL_{50}$ and post-IR $IRSL_{200}$ bleaching behaviour for all samples subjected to the bleaching experiment. Each data point indicates the average normalised L_x/T_x calculated for all grains at every bleaching step. All uncertainties indicate one standard error.

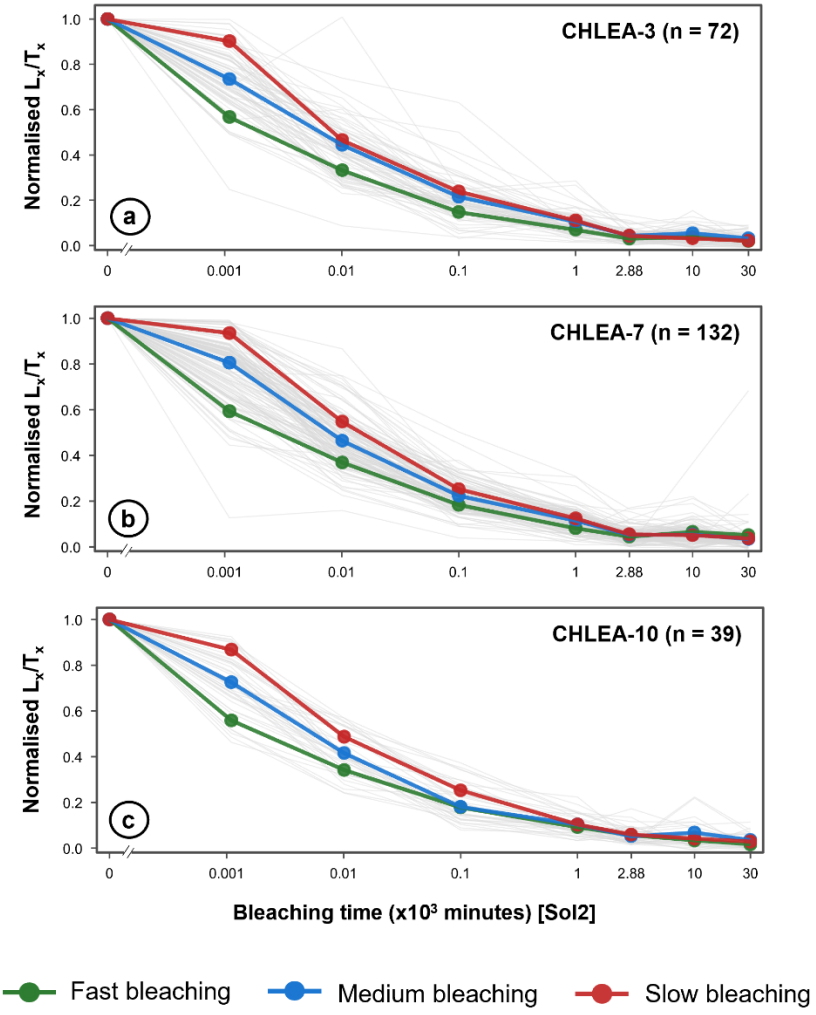

Fig. S8: Normalised luminescence signal (L_x/T_x) as a function of the Sol2 bleaching time for (a) CHLEA-3 (n = 72 grains), (b) CHLEA-7 (n = 132 grains), and (c) CHLEA-10 (n = 39 grains). Semi-transparent grey lines represent the signal decay trajectories of individual single-grains. To quantify bleaching heterogeneity, grains were classified into three groups based on their normalised L_x/T_x values at the 1-minute bleaching step: lower quartile representing fast-bleaching grains (green, ≤ Q1), interquartile range representing medium-bleaching grains (blue, Q1–Q3), and upper quartile representing slow-bleaching grains (red, ≥ Q3). Bold coloured lines with markers illustrate the average bleaching trajectory for each quartile group tracked consistently across all subsequent bleaching durations.

S5: Details of microprobe measurement

Over three measurement days, concentrations of all major elements (>1 wt%) remained within 5% of the reference composition for the P&H orthoclase secondary standard, except BaO, which stayed within 10%. Fe_2O_3 and CaO deviated by more than 10%, and their results should be interpreted with caution. The microprobe data were filtered based on the minimum detection limits of K_2O (0.03 wt%) and Na_2O (0.04 wt%), the two key elements involved in the solid-solution relationships among various feldspar phases observed in our samples (Fig. S9a–d). MnO concentrations were below the microprobe's detection limit and were therefore excluded from all analyses. Additionally, filtering was performed to exclude erroneous measurements of major oxide concentrations in K-feldspar grains where the total concentration (wt%) fell outside the range of 100 ± 5 wt%.

Table S7: Measurement details of orthoclase from the P&H standard block as secondary reference material before and after each measurement session to monitor precision and accuracy. The results indicate the mean (± 2 standard deviations) of ten (five before and five after each measurement session) measurement points.

Measurement date	Reference material	Fe_2O_3 (wt%)	Na_2O (wt%)	K_2O (wt%)	BaO (wt%)	MnO (wt%)	SiO_2 (wt%)	CaO (wt%)	Al_2O_3 (wt%)	Total (wt%)
16.12.2024	P&H orthoclase	0.024 ±0.05	1.4 ± 0.4	14.7 ± 0.5	0.1 ± 0.1	0.01 ±0.03	64.2 ± 0.8	0.016 ± 0.032	18.8 ± 0.4	99 ± 1
17.12.2024	P&H orthoclase	0.02 ± 0.042	1.4 ± 0.1	14.5 ± 0.3	0.14 ± 0.07	0.01 ± 0.02	65 ± 1	0.017 ± 0.029	18.7 ± 0.5	100 ± 2
18.12.2024	P&H orthoclase	0.031 ± 0.065	1.4 ± 0.2	14.5 ± 0.3	0.16 ± 0.05	0.01 ± 0.05	65 ± 2	0.013 ± 0.025	18.8 ± 0.7	100 ± 2

Table S8: Limit of detection of microprobe measurements.

Oxides	Fe_2O_3	Na_2O	K_2O	BaO	MnO	SiO_2	CaO	Al_2O_3
Limit of detection (wt%)	0.058	0.04	0.03	0.092	0.05	0.04	0.027	0.04

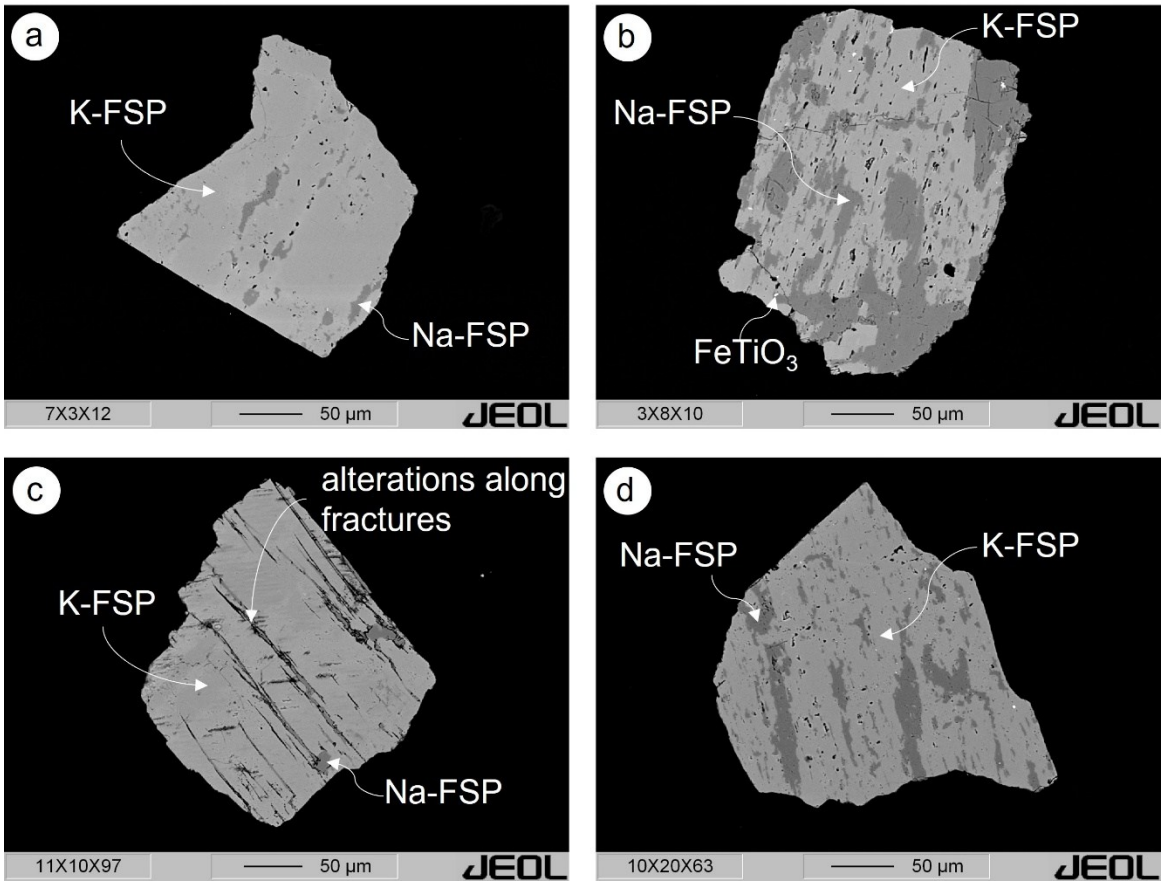

Fig. S9: Electron back scatter images of four selected grains (a–d), one from each sample subjected to the bleaching experiment. Images were captured and the mineralogical composition indicated in the images is based on energy-dispersive X-ray spectroscopy (EDS) analysis performed during microprobe measurement. Na-FSP: Na-feldspar and K-FSP: K-feldspar. Note the alterations present along the fractures (panel c). The number combination at the bottom left of each figure shows the sample number, disc number and the measured grain number. For example, in (a) 7X3X12 means grain number 12 from disc 3 of sample CHLEA-7.

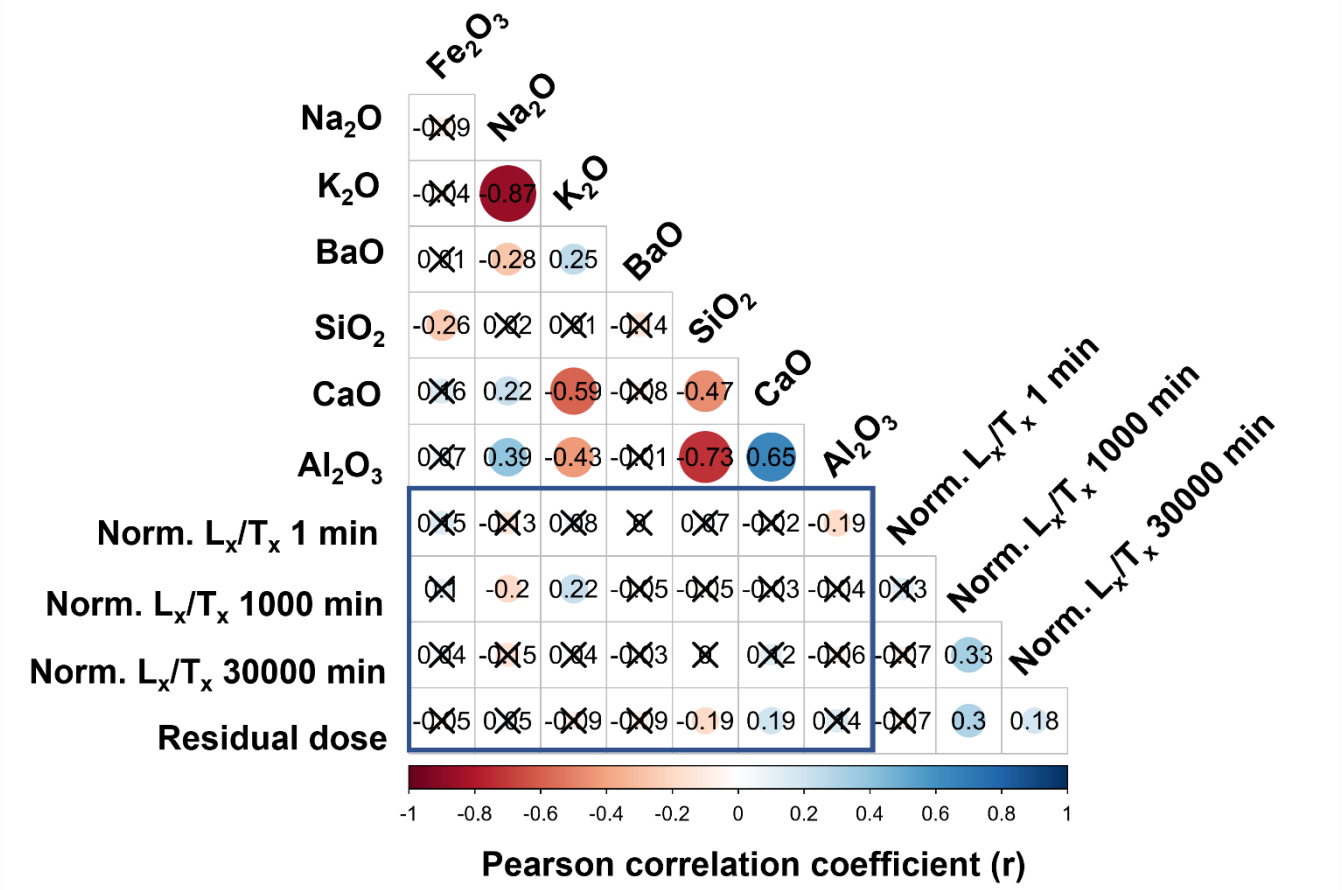

Fig. S10: Correlation matrix showing the correlation between and within grain-specific residual dose (measured dose after 2 days of Sol2 bleaching), normalised L_x/T_x of 1 minute, 1000 minutes, and 30000 minutes bleaching steps and all measured oxides for all four samples subjected to the bleaching experiment. Numbers in the circles represent Pearson correlation coefficient (r) values, and size and colour show the strength of the correlation. The boxes with cross marks represent statistically non-significant correlations with a p-value greater than 0.05. The blue rectangle in the figure marks the correlation between geochemical data and luminescence data.

S6: Laboratory test of natural dose dependency

Table S9: Protocol of the laboratory experiment to test natural dose dependency.

Steps	Actions
1	Dose (0, 30, 60, 120 Gy) above the respective natural doses
2	2 days of bleaching in Sol2
3	Residual dose measurement following the protocol in Table 1

265

Table S10: Residual dose results from feldspar single-grain post-IR $IRSL_{200}$ measurements for samples CHLEA-7 and CHLEA-11 following two days of Sol2 bleaching at four given dose levels administered above the respective natural doses. Column headers are as follows: Given Dose: the dose administered above the natural dose; n (%): the absolute and relative number of accepted grains in the residual dose distribution; $Mean_{Residual}$: the mean residual dose 270 **with one standard error; $Mode_{Residual}$: the modal residual dose with the one-sigma confidence interval in parentheses, derived from bootstrap resampling (n = 1000).**

Sample ID	Given dose (Gy)	n (%)	$Mean_{Residual}$ (Gy)	$Mode_{Residual}$ (Gy)
CHLEA-7	0	132 (33)	9.5 ± 0.4	7.75 (7.07-8.69)
	30	123 (41)	8.5 ± 0.3	6.55 (6.19-9.18)
	60	122 (41)	8.7 ± 0.3	7.57 (7.19-10.28)
	120	119 (40)	8.4 ± 0.3	7.29 (6.82-7.96)
CHLEA-11	0	603 (38)	3.4 ± 0.1	0.96 (0.90, 1.07)
	30	152 (51)	3.1 ± 0.2	1.03 (0.95-1.15)
	60	142 (47)	3.2 ± 0.2	1.26 (1.14-1.43)
	120	131 (44)	3.7 ± 0.3	2.24 (1.73-2.48)

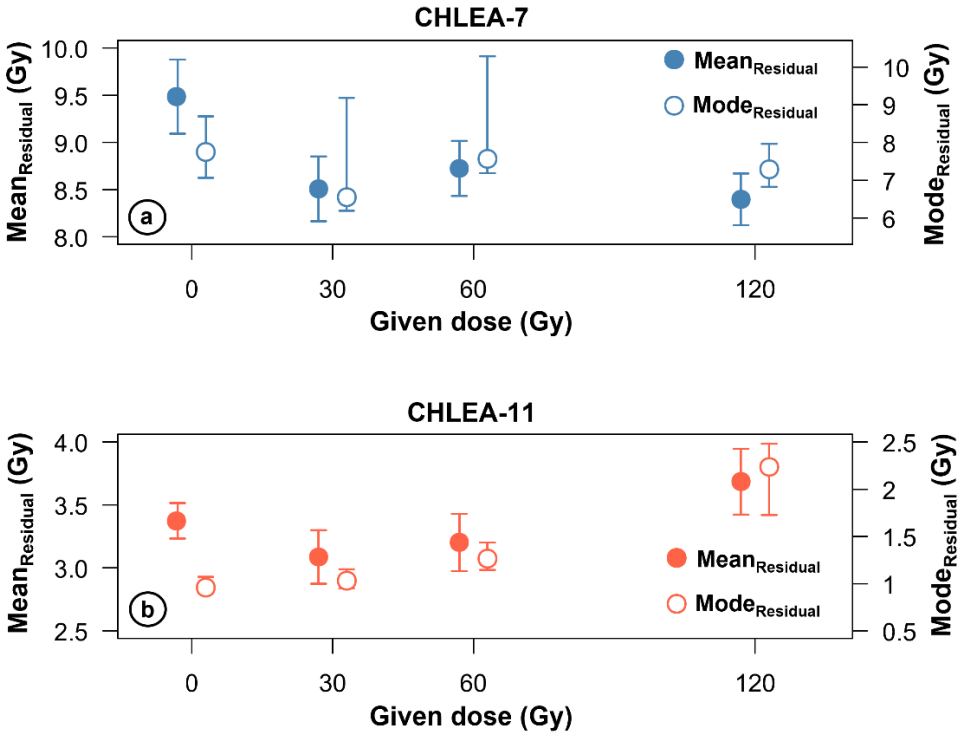

Fig S11: Residual dose estimates (both mean and mode) for samples CHLEA-7 (a) and CHLEA-11 (b) following two days of Sol2 bleaching, obtained from feldspar single-grain post-IR $IRSL_{200}$ measurements at four given dose levels (0, 30, 60, and 120 Gy) administered above the respective natural doses. Filled and open circles represent the mean ($Mean_{Residual}$; left y-axis) and modal ($Mode_{Residual}$; right y-axis) residual doses, respectively. Uncertainties on $Mean_{Residual}$ are expressed as one standard error, and uncertainties on $Mode_{Residual}$ represent one-sigma confidence intervals derived from bootstrap resampling (n = 1000).

S7: Lithological composition and luminescence characteristics

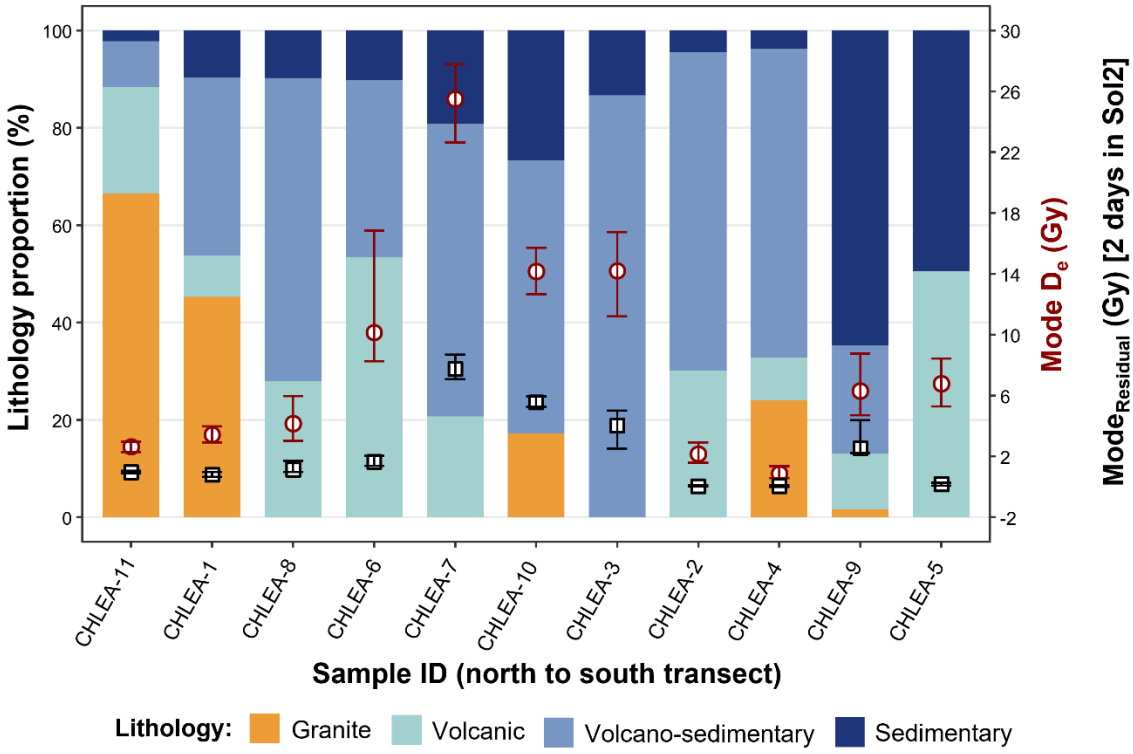

Fig S12: Lithological composition and luminescence characteristics of all eleven catchments in the Southern Central Andes, Chile. Stacked bars show the relative proportions (%) of four lithological categories: Granite, Volcanic, Volcano-sedimentary, and Sedimentary, within each catchment. Superimposed symbols indicate luminescence signal properties: black squares represent the residual dose (measured after two days of bleaching in Sol2) based on the mode of the distribution ($Mode_{Residual}$), while red circles indicate the equivalent dose based on the mode of the distribution (Mode D_e) for each sample. Uncertainties indicate one sigma confidence intervals. Sample IDs (CHLEA) are ordered geographically from north to south.

S8: Test of recuperation dose as a proxy for bleachability

Residual doses of individual grains were compared with their corresponding recuperation doses, which were derived from measurements conducted within the single aliquot regenerative dose (SAR) protocol (Table 1, Step 10: zero-dose measurement following the natural signal). To estimate the recuperation dose, the test dose corrected luminescence response was projected onto the linear segment of the dose-response curve, defined between the origin and the response to the third regenerative dose (~5 Gy). Associated uncertainties were propagated based on the errors of individual measurements.

A subset of recuperation doses yielded negative values, which are interpreted as artifacts likely arising from elevated background-to-signal ratios. To keep the analysis physically meaningful, only positive recuperation dose values were considered. To evaluate the potential of recuperation dose as an indicator of grain-specific bleachability, we conducted a weighted regression analysis between recuperation dose and residual dose. The results of this analysis are summarised in Table S11.

Table S11: Summary statistics of the weighted linear regression fit based on single-grain recuperation dose and residual dose. Note that the n represents the number of positive data points used in the weighted linear regression.

Sample ID	n	Intercept	Slope	Adjusted R^2	p-value
CHLEA-11	534	1.00	0.11	0.00	0.38
CHLEA-1	74	0.35	1.65	0.11	0.00
CHLEA-8	14	2.96	-0.94	-0.04	0.51
CHLEA-6	31	0.62	2.64	0.32	0.00
CHLEA-7	123	3.98	3.50	0.17	0.00
CHLEA-10	39	1.25	4.10	0.35	0.00
CHLEA-3	54	-0.52	2.27	0.07	0.03
CHLEA-2	44	-0.07	0.65	0.07	0.04
CHLEA-4	24	0.08	-0.04	-0.04	0.90
CHLEA-9	28	2.76	0.03	-0.04	0.98
CHLEA-5	23	-0.78	4.49	0.46	0.00

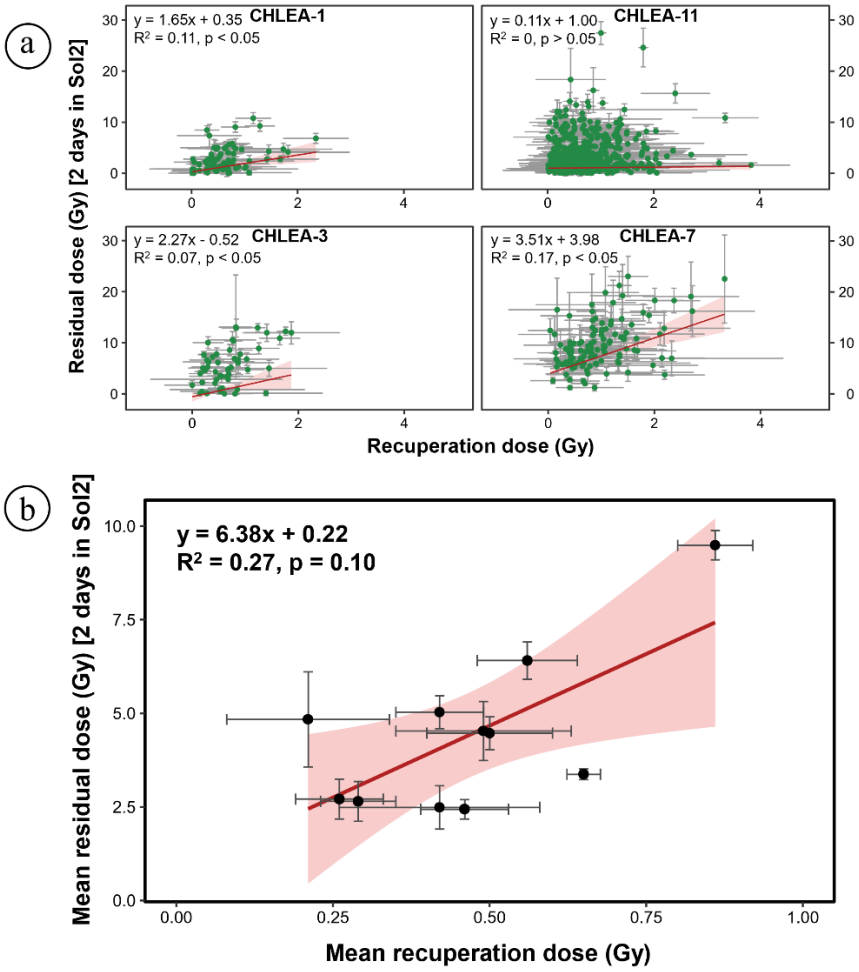

Fig S13: Relationships between residual dose and recuperation dose. (a) Scatter plots showing residual dose versus recuperation dose at single-grain level for four samples (CHLEA-1, CHLEA-11, CHLEA-3, CHLEA-7). Each panel includes the statistics (regression equation, R^2, and p-value) of the fitted linear regression. (b) Sample-averaged residual dose plotted against sample-averaged recuperation dose, with linear regression. The shaded red envelope around the regression line represents a 95% confidence interval. Error bars represent ±1 standard error.

References

Burow, C., 2023. calc_CentralDose(): Apply the central age model (CAM) after Galbraith et al. (1999) to a given De distribution. Function version 1.4.1. In: Kreutzer, S., Burow, C., Dietze, M., Fuchs, M.C., Schmidt, C., Fischer, M., Friedrich, J., Mercier, N., Philippe, A., Riedesel, S., Autzen, M., Mittelstrass, D., Gray, H.J., Galharret, J., 2023. Luminescence: Comprehensive Luminescence Dating Data Analysis. R package version 0.9.21, https://CRAN.R-project.org/package=Luminescence

Burow, C., 2023. calc_MinDose(): Apply the (un-)logged minimum age model (MAM) after Galbraith et al. (1999) to a given De distribution. Function version 0.4.4. In: Kreutzer, S., Burow, C., Dietze, M., Fuchs, M.C., Schmidt, C., Fischer, M., Friedrich, J., Mercier, N., Philippe, A., Riedesel, S., Autzen, M., Mittelstrass, D., Gray, H.J., Galharret, J., 2023. Luminescence: Comprehensive Luminescence Dating Data Analysis. R package version 0.9.21, https://CRAN.R-project.org/package=Luminescence

Carretier, S., Regard, V., Vassallo, R., Aguilar, G., Martinod, J., Riquelme, R., Pepin, E., Charrier, R., Herail, G., Farias, M., Guyot, J.L., Vargas, C., and Lagane, C.: Slope and climate variability control of erosion in the Andes of central Chile, Geology, 41(2), 195-198. https://doi.org/10.1130/G33735.1, 2013.Dietze, M., 2023. plot_KDE(): Plot kernel density estimate with statistics. Function version 3.6.0. In: Kreutzer, S., Burow, C., Dietze, M., Fuchs, M.C., Schmidt, C., Fischer, M., Friedrich, J., Mercier, N., Philippe, A., Riedesel, S., Autzen, M., Mittelstrass, D., Gray, H.J., Galharret, J., 2023. Luminescence: Comprehensive Luminescence Dating Data Analysis. R package version 0.9.21, https://CRAN.R-project.org/package=Luminescence

Gómez, J., Schobbenhaus, C., and Montes, N.E.: Geological Map of South America 2019. Scale 1:5 000000. Commission for the Geological Map of the World (CGMW), Servicio Geológico Colombiano and ServiçoGeológico do Brasil. Paris, France, https://doi.org/10.32685/10.143.2019.929, 2019.

Gorelick, N., Hancher, M., Dixon, M., Ilyushchenko, S., Thau, D., and Moore, R.: Google Earth Engine: Planetary-scale geospatial analysis for everyone, Remote Sens. Env., 202, 18-27, https://doi.org/10.1016/j.rse.2017.06.031, 2017.

Huffman, G.J., E.F. Stocker, D.T. Bolvin, E.J. Nelkin, Jackson Tan (2023), GPM IMERG Final Precipitation L3 1 day 0.1 degree x 0.1 degree V06, Edited by Andrey Savtchenko, Greenbelt, MD, Goddard Earth Sciences Data and Information Services Center (GES DISC), Accessed: 2023-05-17, 10.5067/GPM/IMERGDF/DAY/06

Kreutzer, S., Burow, C., Dietze, M., Fuchs, M.C., Schmidt, C., Fischer, M., Friedrich, J., Mercier, N., Philippe, A., Riedesel, S., Autzen, M., Mittelstrass, D., Gray, H.J., and Galharret, J.: Luminescence: Comprehensive Luminescence Dating Data Analysis, R package version 0.9.23, https://CRAN.R-project.org/package=Luminescence, 2023.

NASA Shuttle Radar Topography Mission (SRTM) (2013). Shuttle Radar Topography Mission (SRTM) Global. Distributed by OpenTopography, https://doi.org/10.5069/G9445JDF. Accessed: 2023-05-01.

Pepin, E., Carretier, S., Guyot, J. L., and Escobar, F.: Specific suspended sediment yields of the Andean rivers of Chile and their relationship to climate, slope and vegetation, Hydrol. Sci. J., 55(7), 1190-1205, https://doi.org/10.1080/02626667.2010.512868, 2010.

RGI 7.0 Consortium, 2023. Randolph Glacier Inventory - A Dataset of Global Glacier Outlines, Version 7.0. Boulder, Colorado USA. NSIDC: National Snow and Ice Data Center. doi:10.5067/f6jmovy5navz. Online access: https://doi.org/10.5067/f6jmovy5navz

Sheather, S.J. and Jones, M.C.: A reliable data-based bandwidth selection method for kernel density estimation. Journal of the Royal Statistical Society: Series B (Methodological), 53(3), 683-690. https://doi.org/10.1111/j.2517-6161.1991.tb01857.x, 1991.

Silverman, B.W.: Density Estimation for Statistics and Data Analysis (1st ed.). Routledge. https://doi.org/10.1201/9781315140919, 1998.